

# 39. Friction and Wear in Micro- and Nanomachines

Maarten P. de Boer, Sameer S. Shroff, Frank W. DelRio, W. Robert Ashurst

The prediction and characterization of multi-length-scale tribological phenomena is challenging, yet essential for the advancement of micro- and nanomachine technology. Here, we consider theoretical underpinnings of multiasperity friction, review various approaches to measure micro- and nanoscale friction and discuss the effect of monolayer coatings to reduce friction and wear. We then overview a theoretical framework known as rate-and-state friction (RSF), in which friction is considered to be a continuous function of velocity and interface state. A microscale test platform that is used to measure friction over multiple decades of velocity and normal load is presented and results are reported. Using the RSF framework, we quantitatively predict and validate the transition from stick-slip to steady sliding, enabling the creation of a microscale kinetic phase diagram. Next, we take a brief look at continued progress in spinning micromachine motor technology. Finally, we discuss wear- and tribopolymer-related phenomena in micro- and nanoswitches, which are promising devices to complement transistors due to their low on resistance and steep subthreshold swing. We anticipate great progress towards reliable, contacting micro- and nanomachines by linking theory and experiment to nano- and microscale tribological phenomena and by improving the testing, materials and processing methods used to characterize these phenomena.

<b>39.1 From Single- to Multiple-Asperity Friction</b> .....	1419
39.1.1 Micromachined Test Structures .....	1420
39.1.2 Monolayer Lubrication in Nano- and MEMS Tribology .....	1422
<b>39.2 Rate-State Friction</b> .....	1422
39.2.1 MEMS Rate-State Friction Test Platform with Decades of Range-in-Control Parameters .....	1423
39.2.2 Rate-State Friction Measurements .....	1425
<b>39.3 Putting MEMS Friction to Use: Making Motors and Friction Instruments</b> .....	1429
39.3.1 Microengines, Pumps and Generators .....	1429
39.3.2 In-situ TEM for Friction Investigations .	1429
<b>39.4 Wear and Tribopolymer Evolution in Micro- and Nanoswitches</b> .....	1430
<b>39.5 Concluding Remarks</b> .....	1432
<b>References</b> .....	1432

Friction and wear phenomena present both challenges and opportunities for micro- and nanosystems. In many possible applications, counterfaces rub against each other. Examples of how this can occur are illustrated in Fig. 39.1, where a close-up of features in a complex locking mechanism [39.1] are shown. Here, a large gear ratio is employed to amplify torque. The gear teeth mesh and rotate about hubs that are made by a five structural level polycrystalline silicon (polysilicon) surface micromachining technology at Sandia National Laboratories, known as the SUMMiT V™

process [39.2]. Features known as dimples are attached under the gears to minimize contact and hence adhesion with the substrate. The dimples also prevent the gears from tilting excessively, as does a guide that is shown at the top right of Fig. 39.1. The output gear meshes with a linear rack that is guided via long rails; rubbing contact is also made there. To move from right to left, a pin must correctly traverse a maze inside the linear rack. If an incorrect decision is made, a ratchet and pawl mechanism (not shown), which also requires rubbing contact, prevents resetting.

In the example from Fig. 39.1, friction is generally a parasitic effect and efforts are directed towards minimizing it. Eliminating friction in micromachines has proven difficult, yet therein lies opportunity. A number of researchers have chosen to take advantage of friction, achieving impressive micro- and nanoscale actuation performance. Microscale stepper motors are linear actuators with step sizes on the order of 10–100 nm. Their actuation forces can reach the mN scale and travel ranges up to hundreds of  $\mu\text{m}$  have been demonstrated. These characteristics compare favorably with the more commonly used comb drives, which typically move 10–20  $\mu\text{m}$  and deliver forces in the low  $\mu\text{N}$  range. Stepper motors are attractive for applications such as positioning for optics [39.3], data storage [39.4, 5] and medicine [39.6]. We also envision that they may be very useful for testing properties of micro- and nanoscale specimens [39.9], and as nanoscale manipulation instruments.

Representative implementations of stepper motors, in which actuation is based on frictional effects, are illustrated in Fig. 39.2. Each of these devices has unique design features, performance tradeoffs and processing requirements. An asymmetric bushing geometry enables the motion of the scratch drive actuator (SDA) in Fig. 39.2a [39.7]. The layout and the drive signal for the SDA are simple, the device area is small ( $\approx 30 \mu\text{m} \times 100 \mu\text{m}$ ), the applied voltage is moderate (30–100 V depending on layer thicknesses), the unidirectional travel distance is 500  $\mu\text{m}$  or more [39.10] and the force output is reasonably large (tens of  $\mu\text{N}$ ) [39.7]. A model that predicts operating voltages has been developed, but it does not treat frictional forces [39.11]. The shuffle motor [39.12] and nanotractor [39.13] designs place voltage-controlled clamps at the ends of an actuator plate, enabling bidirectional motion. These actuators can be modeled well and the nanotractor, pictured in Fig. 39.2b, achieves a theoretical maximum force value of  $F_{\text{max}} = 0.5 \text{ mN}$  [39.13]. A subsequent design known as the  $\mu\text{Walker}$  with two degrees of

freedom has been demonstrated [39.8, 14] as shown in Fig. 39.2c. Both the nanotractor and the (2-D)  $\mu\text{Walker}$  achieve other theoretical expectations including step size on the order of tens of nm and average velocity proportional to step frequency up to the mm/s range. The 2-D  $\mu\text{Walker}$  is produced in a four mask process with two layers of structural polysilicon. It takes advantage of a  $\text{Si}_3\text{N}_4$  coating for in-plane isolation of voltage applied to the clamps, and also as a mechanical layer to enhance wear characteristics. The nanotractor is fabricated in the SUMMiT V<sup>TM</sup> process and is also a model friction test structure.

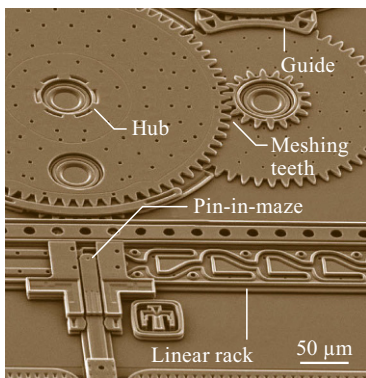


**Fig. 39.1** Rubbing surfaces occur in many micromachine applications and pose a reliability challenge. This figure shows an example of complex mechanical logic

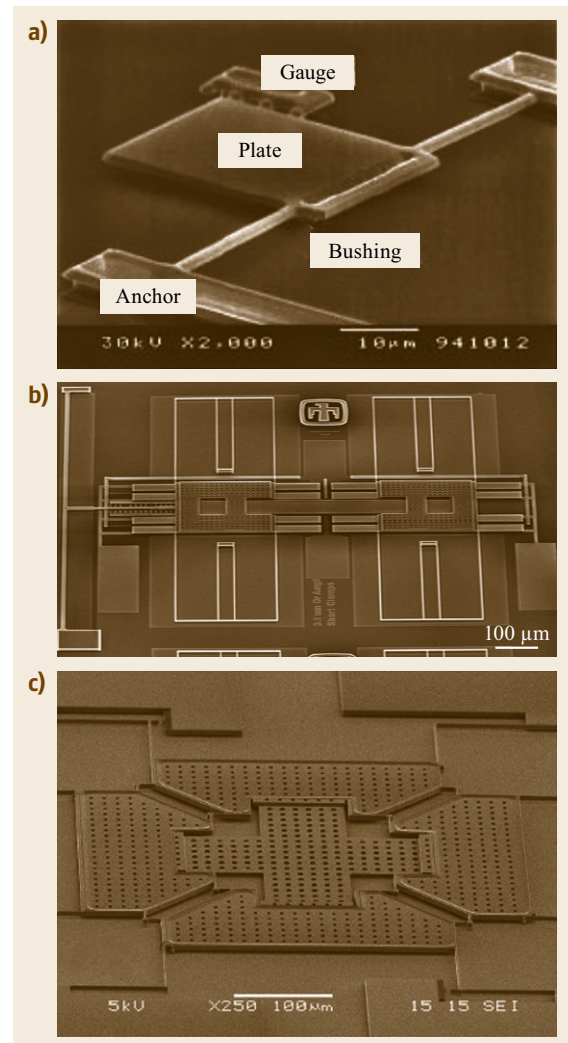


**Fig. 39.2a–c** Rubbing surfaces can also be used to create powerful actuators such as a (a) scratch drive actuator (after [39.7], © IEEE by permission) (b) nanotractor and (c) 2-D  $\mu\text{Walker}$  (after [39.8], © Koninklijke Bibliotheek, Den Haag)

In the following sections, we shall describe the theoretical underpinnings of multiasperity friction, micromachined test structures to measure friction and monolayer coatings that have been used to reduce friction on microelectromechanical systems (MEMS). The major focus of this chapter will then be on testing, metrology, friction and wear.

## 39.1 From Single- to Multiple-Asperity Friction

According to Amontons' empirically deduced law [39.15], the friction force,  $F_f$ , is directly proportional to the applied normal load,  $F_n$ , and independent of the apparent contact area, as described by

$$F_f = \mu F_n, \quad (39.1)$$

where  $\mu$  is the coefficient of friction. For surfaces at rest, the coefficient of static friction is denoted as  $\mu_s$ , while for surfaces in relative motion, the coefficient of dynamic friction is denoted as  $\mu_d$ .

Upon considering two surfaces in mechanical contact, it becomes clear that real surfaces are rough on the microscale, consisting of many peaks and valleys. Thus, the *real* contact area  $A_r$  between two surfaces is actually defined by the highest peaks, also known as asperities, and is much less than the *apparent* contact area  $A_a$ . *Bowden and Tabor* [39.16] presented the idea that friction is related to the real (as opposed to apparent) area of contact via two basic mechanisms: shearing and plowing. Shearing refers to the force required to break the junctions at contacting asperities, while plowing represents the force needed for a hard asperity to displace softer material. In the absence of plowing (i. e., for two materials with roughly the same hardness as is usually the case in micromachined materials), friction is directly proportional to the real contact area via

$$F_f = \tau A_r, \quad (39.2)$$

where  $\tau$  is the shear strength of the contact. Hence Amontons' law is recovered if  $A_r$  is proportional to normal load.

The proportionality between real contact area and applied load, however, seems to disappear for two asperities in *elastic* contact. *Hertz* [39.17] provided the first analysis of the stress distribution and displacement at the interface of two elastic spheres, which can be simplified to a sphere in contact with a flat surface. The total load  $F_n$  compressing a sphere of radius  $R$  into a flat surface can be related to the contact area  $A_r$  by

$$A_r = \pi \left( \frac{3F_n R}{4E^*} \right)^{\frac{2}{3}}, \quad (39.3)$$

where the combined elastic modulus of the two contacting surfaces

$$E^* = \left( \frac{1 - \nu_1^2}{E_1} + \frac{1 - \nu_2^2}{E_2} \right)^{-1}.$$

*Johnson, Kendall, and Roberts* (JKR) later observed that the contact area between two rubber spheres was larger than that predicted by the Hertz theory and developed a model to account for the surface forces at the interface [39.18]. The model was based on a balance between the stored elastic energy, the mechanical energy in the applied load, and the surface energy. *Derjaguin, Muller, and Toporov* (DMT) used a thermodynamic approach to consider the molecular forces in and around the contact zone [39.19]. Unlike the JKR approach, the profile of the sphere outside of the contact area was assumed to be Hertzian (i. e., the surface forces are small enough that their effect on the deformation of the sphere can be neglected). Initially, the models seemed to contradict each other. *Tabor* [39.20] determined that the models represent the extreme ends of a spectrum, and developed a parameter  $\mu_T$  to span the spectrum. Accordingly, the JKR theory is suitable for elastically compliant materials with a large radius and surface energy  $w$ , while the DMT theory is appropriate for elastically stiff materials with a small radius and surface energy. *Maugis* [39.21] later developed a semi-analytical solution using a Dugdale approximation; the transition from DMT to JKR was described in terms of the parameter  $\lambda$ , which is related to  $\mu_T$  via  $\lambda = 1.16\mu_T$ . Figure 39.3 illustrates the relationship between  $A_r$  and  $F_n$  for all of these models. In the presence of attractive forces, the contact area increases at a given load, which increases the friction force, as depicted by (39.2). More importantly, all of the models exhibit a nonlinear relationship between real contact area and applied load, contradicting expectations from Amontons' law.

A number of researchers [39.22–24] have successfully used the aforementioned single-asperity relationships to model friction measurements taken via friction-force microscopy (FFM). However, micro- and nanodevices fabricated using surface micromachining techniques often have contacting surfaces with nanometer-scale surface roughness. As a result, it be-

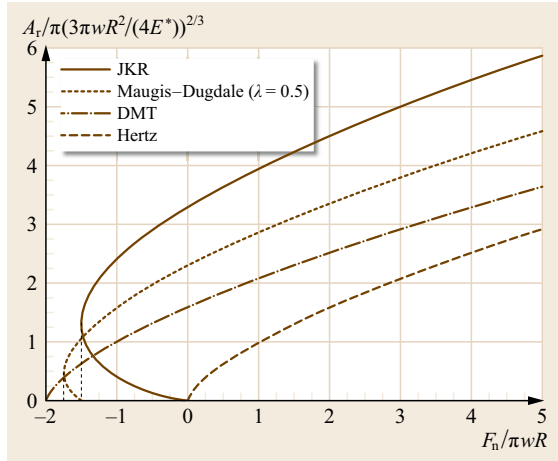


**Fig. 39.3** Normalized  $A_r$ - $F_n$  curves for the Hertz, DMT, Maugis-Dugdale, and JKR contact models. As the transition parameters  $\mu_T$  and  $\lambda$  increase from zero to infinity, there is a continuous transition from the DMT to the JKR regime. In the absence of adhesion, all of the models approach the Hertzian case

comes important to develop *multiple*-asperity contact models to elucidate the impact of surface topography on the relationship between contact area and applied load. In the simplest case, the rough surface consists of a series of identical asperities all at the same height, as shown in Fig. 39.4a. Here, the applied load is divided evenly among all of the contacting asperities, which results in  $A_r \propto F_n^{2/3}$ . Archard [39.25, 26] improved on this idea by considering a *uniform* distribution of spherical asperities (radii of curvature  $R_1$ ) in contact with a rigid flat surface as shown in Fig. 39.4b. For elastic deformation,  $A_r \propto F_n^{4/5}$ . To examine multiscale roughness, a second set of protuberances (radii of curvature  $R_2$ ) can be evenly distributed over the surface of the existing spheres, such that  $R_2 \ll R_1$ , as shown in Fig. 39.4c. In this case,  $A_r \propto F_n^{14/15}$ . With even smaller protuberances of radius  $R_3$ , as shown in Fig. 39.4d, the relationship becomes  $A_r \propto F_n^{44/45}$ . This indicates that proportionality between area and load is not necessarily the result of plastic flow in the contact zones, as originally proposed, but can be due to elastic contact between rough surfaces.

Greenwood and Williamson (GW) considered a *statistical* distribution of  $N$  asperities with constant radius of curvature  $R$  in contact with a flat surface [39.27]. For a Gaussian distribution of asperity heights,  $A_r$  is almost exactly proportional to  $F_n$ . Fuller and Tabor [39.28] extended the GW model for JKR contacts to study rough surface adhesion and defined the adhesion parameter  $\theta$ , which represents the competition between the compressive forces exerted by the higher asperities and

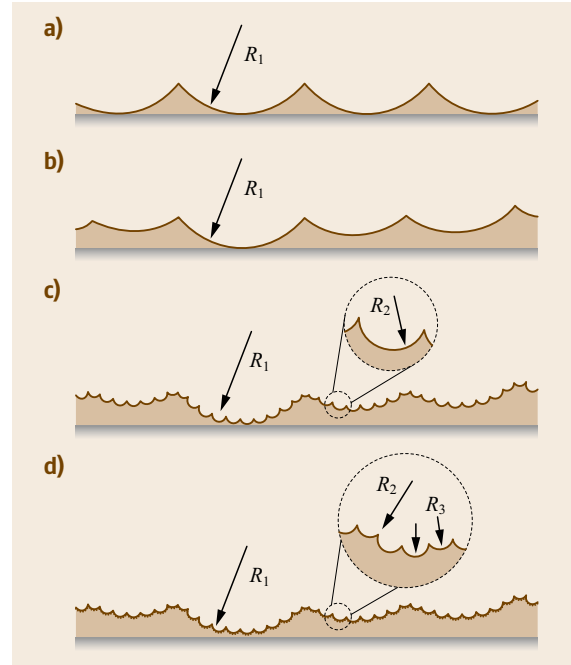


**Fig. 39.4a-d** Multiple-asperity models (after [39.26]). Assuming elastic deformation, the relationship between the contact area  $A_r$  and the applied load  $F_n$  are (a)  $A_r \propto F_n^{2/3}$ , (b)  $A_r \propto F_n^{4/5}$ , (c)  $A_r \propto F_n^{14/15}$ , and (d)  $A_r \propto F_n^{44/45}$ . In general, the index  $n$  in the relationship  $A_r \propto F_n^n$  ranges from  $2/3$  for a series of asperities at the same height to  $\approx 1$  for a multiple-asperity surface with several sets of protuberances

the adhesive forces acting between the lower asperities (analogous to the Tabor parameter). In a similar manner, Maugis [39.29] extended the GW model for DMT contacts. For infinite  $\theta$  (work of adhesion  $w = 0$ ), the Maugis theory is equivalent to the GW model and  $A_r \propto F_n$ . On the other hand, as  $\theta$  decreases ( $w$  increases), the relationship between the contact area and applied load becomes more nonlinear. More advanced theories that extend these ideas are under development [39.30-32].

### 39.1.1 Micromachined Test Structures

From this survey of multiple-asperity contact models, we see that adhesive forces and asperity distribution can significantly impact the relationships between friction force, contact area and applied load. Therefore, although widely observed, Amontons' law is not necessarily expected. While there are techniques in place to convert topographic data from real surfaces into Gaussian asperity distribution data [39.33], it is unclear as to whether these statistical models accurately represent the surface topography [39.32]. Therefore, it becomes nec-

essary to fabricate micromachined test structures that can be used to measure friction directly. Moreover, micromachined structures are appropriate test vehicles for studying friction and wear because their performance will reflect any effects that are due to details of the fabrication process. These include technologically relevant issues such as the effect of sidewall slope on vertical surfaces, surface roughness and the ability to coat micromachined structures with friction-reducing coatings in spite of sometimes tortuous access paths.

One of the earliest systematic studies of microscale friction was carried out by *Howe* et al. at the University of California, Berkeley [39.34]. Since then, a number of researchers have investigated this critical issue using a variety of techniques and devices. A common approach is to design a moveable beam that can be brought into contact and slid against a counter surface [39.35–41]. An example from [39.39] is shown in Fig. 39.5a,b. The measurements from this study showed that statistical contact models as described above may not apply to lightly loaded, small apparent contact areas in MEMS. This is because such models would predict less than one contact within the contact area! The researchers also found that adhesion between the surfaces must be recognized as an important contribution to the applied normal load. Most microdevice friction work has involved so-called *sidewall* devices such as this one, where the contacting surfaces are the result of an etching procedure and may have vertical striations and significant directional anisotropies. The topography of sidewalls is influenced by lithography, etching and grain boundaries, as seen in Fig. 39.5c [39.42], and often exhibits significantly higher roughness than in-plane surfaces where topography is primarily determined by grain growth phenomena.

*Timpe* and *Komvopoulos* [39.40] developed a sidewall microscale friction device that involved a push drive and a shear drive. Testing of the device consisted of first loading the contact and then shearing the newly formed interface while monitoring the position of the shear drive with a charge-coupled device (CCD) camera, with a spatial resolution of about  $0.3\ \mu\text{m}$ . It was shown that the engineering coefficient of friction exhibited a nonlinear dependence on contact pressure that was unique to the testing environment; higher friction was observed at higher humidity levels. Further, the adhesion forces, significant at the microscale, added substantially to the friction when the external load was comparable to the adhesion force [39.40].

Frenken and co-workers recently developed a similar sidewall device, but included an on-device, real-time, electrical capacitance readout mechanism for high-resolution displacement measurement (about  $4\ \text{nm}$  peak-to-peak noise sensitivity). Their device, called the

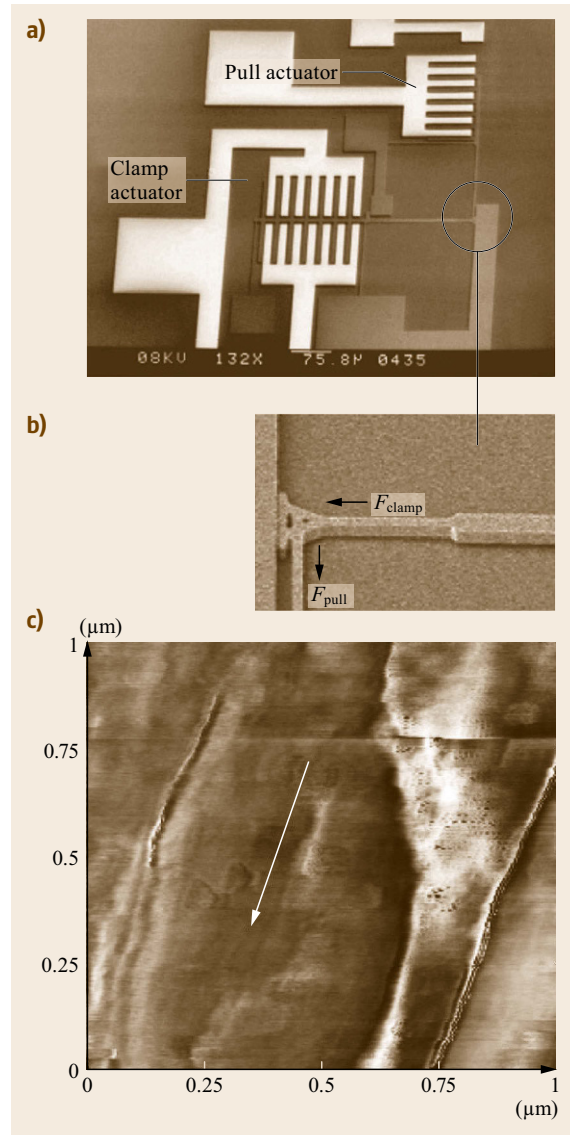


**Fig. 39.5** (a) A MEMS test structure (b) designed to measure sidewall friction (after [39.39], © VSP). (c) Topographical image of a sidewall surface, where the RMS roughness is  $40\ \text{nm}$  (after [39.42], © Xavier by permission)

*Leiden MEMS Tribometer*, consists of two orthogonally oriented comb drives that are used to position a test slider against a fixed surface. The comb drives are used to generate loading and shearing forces on the contact surface. They indicated two regimes in the friction behavior depending on the load. For the low-loading regime, a wearless stick-slip phenomenon is observed that is repeatable over many cycles but stochastic in position and presumably related to the details of the topography. In the high-loading regime, wear was ob-

served, and although the stick-slip behavior exhibited in the low-load regime disappeared, the motion was not smooth, as ongoing wear processes altered the surface topography and changed the contact mechanics [39.38].

### 39.1.2 Monolayer Lubrication in Nano- and MEMS Tribology

While the results in the previous section are of interest, the effects of monolayer coatings, which significantly reduce friction, were not studied. It has been well established that monolayer lubricants are effective at reducing friction at the nanoscale. Much of this knowledge has been achieved through nanotribology experiments involving atomic-force microscopy (AFM) [39.43, 44] or a surface-forces apparatus (SFA) [39.45], where ideal systems (i. e., pristine environments, single-crystal substrates, perfect monolayers, etc.) are employed to probe fundamental aspects of friction phenomena using single-asperity contacts.

Nanotribology studies have shown significant (and sometimes conflicting) impact of monolayer thickness (i. e., precursor chain length) and terminal group on friction [39.46–49]. Similar to rough surfaces, there are two basic phenomena involved in single-asperity friction: plowing and shearing [39.44]. With regard to monolayer coatings, plowing refers to the action of the asperity tip deforming the monolayer thereby dissipating energy by introducing chain defects that may elastically relax after the tip has passed, while shearing refers to the localized disruption of intermolecular forces as a result of the shear interaction of the film surface with the tip. Some researchers report an increase in friction as chain length increases [39.50], while others report a decrease in friction [39.48]. These conflicting findings suggest that additional experimental factors contribute to the frictional behavior of monolayer films, and the operating conditions must be considered in the friction study.

As discussed above, the friction force may be proportional to the true contact area, leading to a nonlinear dependence of friction with load. This has been supported by experimental data for inorganic materials. However, in many studies of organic monolayers, a linear relationship is found [39.46, 48, 51–53]. This could be attributed to plastic deformation, to multiple contacting nanoasperities on the single-AFM tip or to vis-

coelastic deformation during the sliding. It is important to note that many of the fundamental mechanistic studies of nanoscale friction have involved high-modulus inorganic materials with similar bulk and surface properties. Since monolayers are comparatively compliant materials, usually deposited on a stiff material, the validity of applying findings from such fundamental studies to monolayer systems can be questioned. Another aspect to consider is that deviation from linearity as in the JKR model [39.18] may be small and experimentally obscured for low loadings, typical of AFM studies [39.44]. Recently, a continuum thin-coating theory was developed to address these issues [39.54, 55].

Some researchers have successfully applied monolayer films to micromachines for the purpose of studying their effects on friction [39.13, 56–59]. The most convenient monolayers to apply to polysilicon microdevices involve silane-based linking reactions with the oxide layer present on the surface. From the silane class of materials, one of the most commonly studied monolayer film is that produced by octadecyltrichlorosilane (OTS). This particular film has received much attention in the literature due to its self-assembly characteristics [39.60]. Work using AFM has shown that the friction behavior of the film is dependent on the local 2-D phase (liquid expanded or liquid condensed) at the asperity contact [39.61] and that liquid-condensed phases are likely to be associated with grain boundary areas for polysilicon devices [39.62]. It is generally accepted by the MEMS community that OTS and other low-friction monolayer boundary lubricant films reduce the friction on microdevices when properly integrated and applied to the device. For example, a factor of  $\approx 4$  reduction in friction was reported at 100 nN normal load for self-mated OTS versus self-mated silicon surfaces [39.63].

The findings assembled from uncoated and coated sidewall devices have significant value to the MEMS community and provide guidance on how to more reliably design and operate microdevices. However, statistical contact mechanics models, which rely on numerous contacts, do not apply because of the small contact areas and nonvertical nature of sidewall etching. Rather, an interface with uniform loading over a large area of in-plane (horizontal) surfaces during friction testing is needed.

## 39.2 Rate-State Friction

Clearly, it would be interesting to link single-asperity measurements made by nanotribologists to multiasperity measurements made by MEMS tribologists. This

would involve a detailed understanding of the surface properties, loading characteristics and topography. Indeed, asperity radii of polycrystalline silicon are on

the order of 20–200 nm, in the same range as AFM tips. At the macroscale, friction measurements on kg-scale masses have revealed complex behavior including aging, velocity dependence, and stick-slip to steady-sliding bifurcations. From these, a phenomenological framework known as rate-state friction (RSF) has been advanced [39.64–68]. This development derives from detailed measurements with various combinations of springs, puller velocities and normal loads, and applies to a wide range of materials from rock [39.65] to cardboard [39.66] to plastic [39.69]. The phenomenology invokes the notion of contact rejuvenation and requires the solution of coupled differential equations in terms of rate (instantaneous velocity) and state (interface order or age) variables [39.70, 71]. Quite possibly, microscale friction will have similar dependencies. As an initial effort to explore some of these potential dependencies, we recently developed a platform to study whether RSF applies to this scale, where a typical mass is on the order of  $10^{-10}$  kg.

Amontons' law states that friction is independent of load, while Coulomb's law states that dynamic friction is lower than static friction, but independent of velocity. Long ago, *Desaguliers* [39.72] observed that static friction tends to increase with time. RSF links these empirical observations and postulates that the coefficient of friction  $\mu$  is a *continuous* function of state and time. Various functional forms have been proposed. The *Ruina–Dieterich* [39.68, 73, 74] *slip* law can be written as

$$\mu(\psi, \dot{x}) = \mu_0 + A \ln \left( 1 + \frac{|\dot{x}|}{v_c} \right) + B \ln \left( 1 + \frac{\psi}{\psi_c} \right), \quad (39.4)$$

where  $\psi$  represents the interface state,  $\dot{x}$  the instantaneous block velocity (the overdot indicates the derivative with respect to time),  $\mu_0$  is a constant,  $A$  and  $B$  are respectively velocity strengthening and aging coefficients, and  $v_c$  and  $\psi_c$  are, respectively, velocity and time cutoffs. A coupled equation describes how  $\psi$  evolves with time. The *Dieterich–Ruina* [39.68, 73] *aging* law is

$$\dot{\psi} = 1 - \frac{|\dot{x}| \psi}{d_c}. \quad (39.5)$$

At rest,  $\dot{x} = 0$ , and hence  $\psi$  is time. At constant velocity (steady sliding at steady state),  $\dot{x} = v_p$ , and  $\psi = d_c/v_p$ , where  $d_c$  is a memory length on the order of the diameters of contacting asperities in dry systems. Referring to the (1-D schematic in Fig. 39.6 with a puller at position  $x_p$  moving at velocity  $v_p$ , a spring with constant  $k$  and block of mass  $m_b$  subject to normal load  $N_b$ , we write

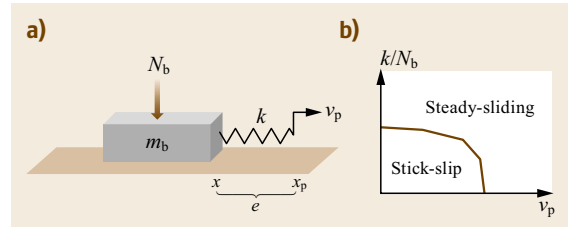


**Fig. 39.6** (a) A puller moving at velocity  $v_p$  causes a block of mass  $m_b$  subject to normal load  $N_b$  to slide via a spring with constant  $k$ . (b) A schematic kinetic friction phase diagram indicating the block response as a function of  $v_p$ ,  $k$  and  $N_b$  in the stick-slip or steady-sliding regimes

the block's equation of motion as

$$m_b \ddot{x} = k(x_p - x) - F_0, \quad (39.6)$$

where the friction  $F_0 = \mu N_b + c\dot{x}$ , and  $c$  is a viscous damping coefficient.

### 39.2.1 MEMS Rate-State Friction Test Platform with Decades of Range-in-Control Parameters

With a test platform as schematically illustrated in Fig. 39.6a, the coefficients in (39.4) can be found in principle. In order to do so, however, it is necessary that  $v_p$ ,  $k$  and  $N_b$  be varied over a wide range as friction varies only slowly with velocity. While this is relatively straightforward to accomplish in macroscale experiments, its design and implementation at the microscale involves many considerations. The overarching objective in creating this apparatus is to determine quantitatively a full response of the system in  $[v_p, k, N_b]$  space using (39.4) and (39.5). One important outcome would be prediction of the stick-slip to steady sliding bifurcation line as seen in Fig. 39.6b. This would demonstrate that a microscale interface can have a predictable sliding response. Further, once the coefficients are known, in principle the response to any velocity or normal load stimulus can be known.

Figure 39.7 shows the microscale platform we have developed in pursuit of this objective [39.75]. A thermal actuator (TA) [39.76–78] is chosen as the puller. While its displacement versus voltage characteristic is nonlinear, it has the advantage that when voltage is applied, the time to achieve the final displacement value is governed by a thermal time constant,  $\tau_H$ . When a voltage  $V_{TA}$  as in Fig. 39.7a is initially applied across the TA legs, a nonzero shuttle velocity is achieved almost instantaneously ( $\approx 0.5 \mu\text{s}$ ), but decays exponentially as the final displacement position is reached. In order to achieve a constant velocity,  $V_{TA}$  is continuously

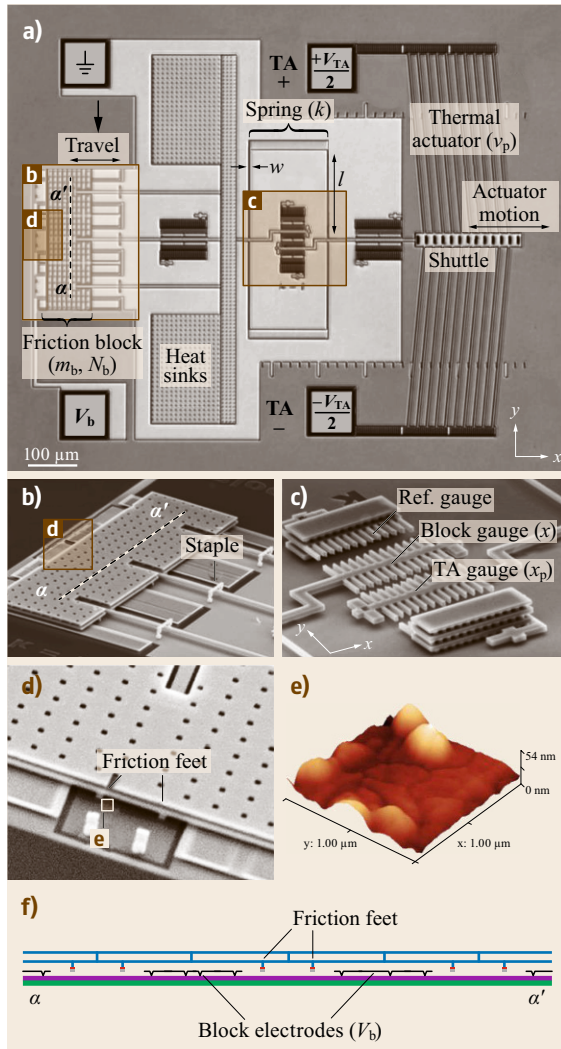


**Fig. 39.7** (a) Optical image of a fabricated and released test platform with the basic components shown in Fig. 39.6 labeled. Here  $k = 1 \mu\text{N}/\mu\text{m}$ . Boxes indicate details shown in the corresponding figure parts (b–e). (b) SEM image of the friction block. Cross section  $\alpha\text{--}\alpha'$  is labeled and shown in (f). The staple minimizes deflections during the release process and plays no role during testing. (c) SEM image of the displacement gauges used for position measurement. (d) SEM image showing two of the six friction feet below the friction block (shown from a different perspective than indicated in the inset of (b)). (e) AFM scan of the countersurface below the friction feet shown in (d). The scan width is approximately half the width of the friction feet. (f) Schematic of cross section  $\alpha\text{--}\alpha'$  showing the electrically grounded friction feet and block actuation electrodes to apply electrostatic normal load

increased after a small fraction of  $\tau_H$ . In detail, a training algorithm known as iterative learning control (ILC) [39.79] is applied to reach the desired velocity in a time on the order of  $1/20$  of the time it takes to travel along the  $\approx 10 \mu\text{m}$  travel range. With ILC, we have trained the actuator to move at velocities from  $0.1$  to  $3000 \mu\text{m/s}$  with  $\approx \pm 10\%$  control [39.75]. Using ILC, the actuator can also be trained to change velocity instantaneously [39.80].

Another important feature of this design is that the TA legs are much stiffer than  $k$ , so the shuttle's motion is independent of whether it is pulling a sliding block or not. The spring itself is labeled in Fig. 39.7. It consists of four fixed-guided beams and its constant  $k$  is determined by their width,  $w$ . By varying  $w$ , designs with  $k = 0.1, 1, 10$  and  $100 \mu\text{N}/\mu\text{m}$  have been fabricated and tested. The TA is thermally isolated from the friction block. Its temperature is  $\lesssim 2^\circ\text{C}$  above the substrate temperature [39.81].

The block's mass is  $3.6 \times 10^{-10} \text{kg}$ . Its gravitational normal force is negligible. The applied normal force is due to two main contributions: electrostatic loading  $F_{el}$  and adhesion,  $F_{adh}$ . Hence

$$N_b = F_{el} + F_{adh} . \quad (39.7)$$

The block is designed with nominally flat feet that contact the substrate over a nominal area of  $A_{nom} = 1000 \mu\text{m}^2$ . Electrodes between the feet are used to apply the voltage to deliver  $F_{el}$ . The value for  $F_{adh}$  will be seen to be  $\approx 1.6 \mu\text{N}$ . As measured by tapping mode AFM, the roughness of the combined top and bottom surfaces is about  $8 \text{nm RMS}$  while the asperity radius of curvature is  $35 \text{nm}$ . According to *Greenwood–Williamson* contact mechanics [39.27], the interface makes at most tens of contacts for the range of  $N_b$  values applied here.

The displacement gauge that is used for metrology is in the middle of the spring. Vernier scales are monitored optically through a  $50\times$  microscope objective with a high-speed camera at rates as high as  $200\,000 \text{fps}$  (frames per second). The images are analyzed using subpixel interpolation, with a resulting resolution of  $\pm 2 \text{nm}$ . The spring force is simply  $k\Delta e$ , where  $\Delta e$  is the spring extension.

The experimental data that follows was measured using the Fig. 39.7 test platform coated by a  $1.2 \text{nm}$ -thick monolayer coating (tridecafluoro-1,1,2,2-tetrahydrooctyl-*tris*(dimethylamino)silane,  $\text{CF}_3\text{C}_5\text{F}_{10}\text{C}_2\text{H}_4\text{Si}(\text{N}(\text{CH}_3)_2)_3$ , FOTAS) deposited from the vapor phase [39.82]. The 8-carbon chain molecule has a sufficiently high vapor pressure to allow vapor-phase deposition, which makes it highly reproducible in a manufacturing setting. However, it is too short to

form a self-assembled monolayer; rather the chains attached to the surface are believed to be somewhat disordered [39.83]. This lack of order may play an important role in the effects reported below.

A wear test was first conducted. In this test, with  $F_e = 5$  or  $250 \mu\text{N}$ , it was seen that  $\mu \approx 0.3$  remained stable for 20 000 cycles for FOTAS-coated devices. For uncoated devices,  $\mu \approx 0.65$  at  $F_e = 5 \mu\text{N}$  was also stable up to 10 000 cycles. In comparison, RSF tests require approximately 100 trials from a given device for complete characterization. Therefore, we can be optimistic that wear is not an issue with respect to assessing RSF with this test platform. We attribute the relatively low wear rate to the lightly loaded interface in which different asperities share the load over the sliding travel distance.

### 39.2.2 Rate-State Friction Measurements

#### Transition from Steady Sliding to Stick-Slip

We pull the block at puller speed  $v_p = 1 \mu\text{m/s}$  using a spring constant  $k = 10 \mu\text{N}/\mu\text{m}$  while applying electrostatic load  $F_e$ , and measure elongation  $e$ . The camera framerate is 300 fps, corresponding to a frame every 3.3 nm of puller position. The data in Fig. 39.8 begin at  $F_e = 0 \mu\text{N}$ . There, the extension is approximately constant. At  $F_e = 0.3 \mu\text{N}$ , the extension exhibits somewhat greater noise. At  $F_e = 0.58 \mu\text{N}$ , the data exhibit discontinuities in  $e$ , corresponding to slip events, and at  $F_e = 0.90 \mu\text{N}$ , the discontinuities are somewhat larger. Finally at  $F_e = 2.01 \mu\text{N}$ , the response is similar to a classic stick-slip curve. Dashed black lines indicate perfect stick of the block. Hence at  $N_b = 2.01 \mu\text{N}$ , there is frictional creep, but at a slower rate than at the lower  $F_e$  values of  $0.58$  and  $0.90 \mu\text{N}$ . This creep is widely observed [39.66, 83, 84] and is indicative of an avalanche process leading to inertial slip.

A metric to deduce the transition between these regimes must be developed. For  $N_b = 2.01 \mu\text{N}$  in Fig. 39.8, a slip distance  $\delta$  is indicated. If we consider the distribution of  $e$  data for a perfect stick-slip curve, it will be uniform. The standard deviation of the  $e$  data multiplied by  $\sqrt{12}$  will equal the width of the (uniform)  $e$  distribution. We call this product the pseudo-slip distance.

In Fig. 39.9a, we plot the pseudo-slip distance against  $F_e$  for FOTAS-coated and oxide coated blocks. For the former, a small but clear abrupt drop in the pseudo slip distance is seen as  $F_e$  is reduced. We use this drop to estimate the transition from stick-slip to steady sliding. The uncoated block in Fig. 39.9a displays only stick behavior, and there is no abrupt drop in  $\delta$ . Choosing the abrupt drop as a metric, the data in Fig. 39.8 for  $F_e = 0$  and  $0.3 \mu\text{N}$  correspond to steady sliding. We at-

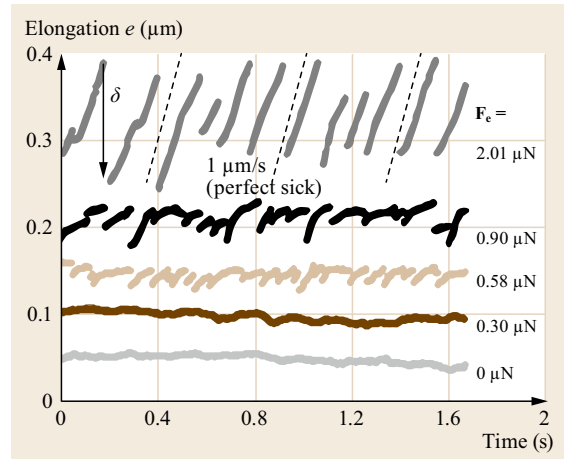


**Fig. 39.8** Spring elongation versus time for increasing  $F_e$ . Here,  $v_p = 1 \mu\text{m/s}$ ,  $k = 10 \mu\text{N}/\mu\text{m}$  and the camera framerate is 300 fps

tribute the small deviations in  $e$  to local differences in the topography encountered, which can be important as there are likely only a few contacting asperities at these low  $F_e$  values.

The maximum extension  $e_{\text{max}}$  for the uncoated and coated blocks is plotted against  $F_e$  in Fig. 39.9b. We fit the data to (39.7), and find values  $F_{\text{adh}} = 2.0$  and  $1.6 \mu\text{N}$  for the two surfaces. With  $A_{\text{nom}} = 1000 \mu\text{m}^2$ , this corresponds to an adhesive pressure of 2.0 and 1.6 kPa, respectively. Such pressures are typical of rough micromachined interfaces, and are attributed not to the contacting asperities but to van der Waals forces across the relatively vast area of surface that are separated by just a few nm [39.85]. These  $F_{\text{adh}}$  values are not interpreted in the context of RSF, but provide a reasonable correction to  $N_b$ .  $F_{\text{adh}}$  sets a lower bound on  $N_b$ . All subsequent measurements discussed are only for FOTAS-coated blocks, and the  $N_b$  value including  $F_{\text{adh}}$  is reported.

We now present five tests: M1–M3, V1 and V2. Here  $M$  stands for measurement, while  $V$  stands for validation.

**Test M1, Friction Versus Velocity.** In the results shown in Fig. 39.10,  $v_p$  is varied from 0.1 to 3000  $\mu\text{m/s}$ , while  $k = 100 \mu\text{N}/\mu\text{m}$  and  $N_b = 14.1 \mu\text{N}$  are held fixed. The stiff spring ensures steady sliding while the relatively high  $N_b$  value gives rise to an extension  $e$  that can be measured well. A frame was taken every 100 nm of travel, which corresponds to 30 000 fps at  $v_p = 3000 \mu\text{m/s}$ . The average and standard deviation of the block velocity are shown in the figure. There is a clear trend in which dynamic friction  $\mu_d$  decreases from 0.1 to  $\approx 300 \mu\text{m/s}$ , and increases thereafter.

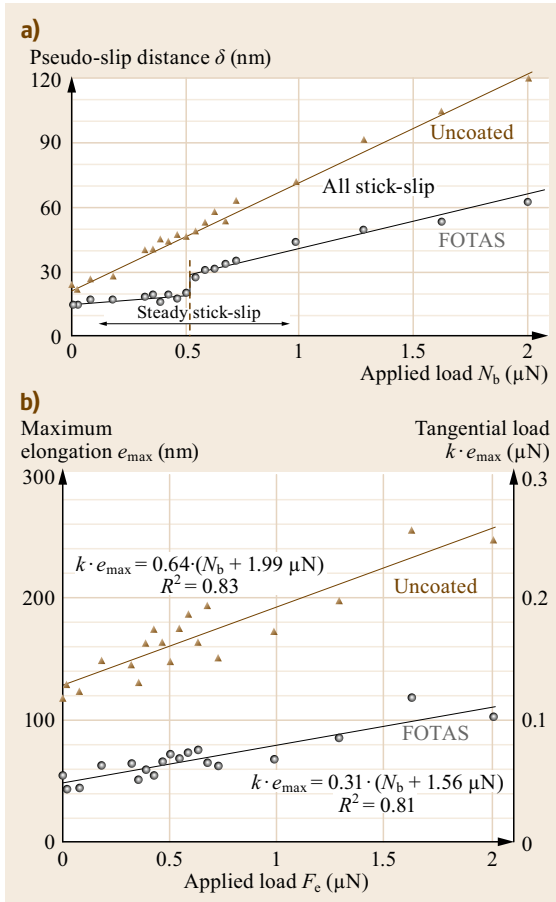


**Fig. 39.9** (a)  $\delta$  versus  $N_b$  for constant  $v_p = 1 \mu\text{m/s}$  and  $k = 10 \mu\text{N}/\mu\text{m}$  for uncoated (triangles) and FOTAS-coated (circles) devices. (b)  $e_{\text{max}}$  versus  $N_b$  for the same data set

Equations (39.4) and (39.5) are used to determine values of  $\mu_0 = 0.19$ ,  $A = 0.013$  and  $B = 0.024$  from this data, as represented by the best fit solid black curve in Fig. 39.10. We also use values of  $v_c = 10 \mu\text{m/s}$ ,  $\psi_c = 10 \mu\text{s}$  and  $d_c = 4.3 \text{ nm}$ . The fit is only weakly dependent of the  $v_c$  and  $\psi_c$  values, and they are chosen such that  $v_p/v_c$  and  $(\psi = d_c/v_p)/\psi_c$  are both  $\gg 1$  in the relevant ranges. Meanwhile,  $d_c$  is determined as shown below. Note that in the fit to (39.4),  $\mu$  initially decreases because  $B > A$ . That is, the asperity contact lifetime decreases as  $v_p$  increases, and hence less aging is responsible for the friction decrease. As  $v_p$  increases, this effect becomes small compared to  $\mu_0$  and the velocity strengthening effect due to  $A$  becomes significant.

**Test M2, Velocity Step Response.** Let us again consider (39.4) and (39.5). Upon an instantaneous change in  $v_p$ , state  $\psi$  remains the same. If  $A > 0$ , we ex-

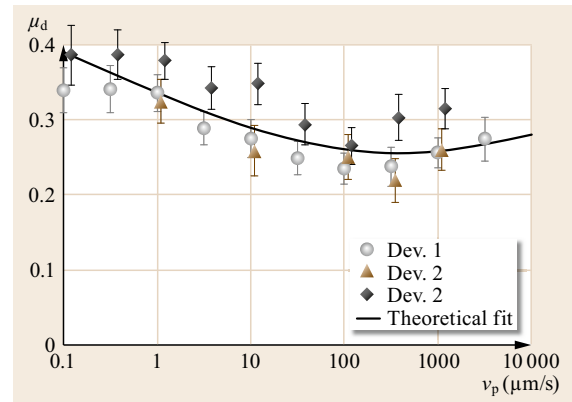


**Fig. 39.10** Dynamic friction coefficient  $\mu_d(v)$  versus actuator pulling velocity in the steady-sliding regime ( $v = v_p$ ). Three devices are shown. Devices 2 and 3 are offset by  $0.1 v_p$  and  $0.2 v_p$ , respectively. Here  $k = 100 \mu\text{N}/\mu\text{m}$  and  $N_b = 14.12 \mu\text{N}$ . Error bars represent one standard deviation of  $\mu_d$  by considering the time-weighted variation in spring elongation of one or more trials

pect a step increase in  $\mu$  equal to  $A \ln(v_{p2}/v_{p1})$ , as shown in Fig. 39.11a. As represented in Fig. 39.11b,  $v_p$  was changed in  $\approx 1 \mu\text{s}$  from 50 to  $1000 \mu\text{m/s}$  with  $k = 100 \mu\text{N}/\mu\text{m}$  and  $N_b = 15.4 \mu\text{N}$ . Here, imaging at 200,000 fps was necessary to capture the transient event, as its duration is  $\approx 20 \mu\text{s}$ . The response data from three different trials is seen in Fig. 39.11c, where it is magnified in the offset on the right. An increase in  $e$  of approximately 5 nm occurs, corresponding to an increase in  $\mu$  of  $ke/N_b = 0.032$ . Equating this with  $A \ln(1000/50)$ , we find  $A = 0.011$ . This is slightly lower than the value  $A = 0.013$  reported above. The discrepancy is because in Fig. 39.11a it is assumed that the block velocity can change instantaneously. This is only possible if the spring is rigid, which would then mean that  $e$  could not be measured. In the actual situation, the state has had some time to change, so  $\mu$  begins to decrease. A full numerical simulation incorporating (39.4)–(39.6) better estimates the value of  $A$  [39.86]. The final value of  $A = 0.013$  from the data in Fig. 39.11c is in good agreement with the value obtained from Test M1.

As indicated by Fig. 39.11a, a fraction of the width of the response pulse can be used to estimate the memory length,  $d_c$ . That width gives  $d_c \approx 0.5 \times (20 \mu\text{s}) \times (1000 \mu\text{m/s}) = 10 \text{ nm}$ . The full numerical simulation, which is optimized to capture the response curve, gives  $d_c = 4.3 \text{ nm}$ . The value from GW contact mechanics is  $d_c \approx 13 \text{ nm}$ . However, it is difficult to get a good measure of asperity radius  $R$  from AFM because of tip convolution effects – the GW calculation may overestimate  $R$ . On the other hand, the monolayer chain length is  $\approx 1.2 \text{ nm}$ . The memory length is associated

with the notion that during sliding, asperities are new when they first make contact, and then age as they slide past each other. The contribution to  $\mu$  is then due to the effective age  $d_c/v_p$ . The implicit assumption is that bonding is instantaneous when new asperities come into contact and subsequently make and break bonds. Poorly ordered monolayers such as FOTAS may reconfigure when brought into contact with a counterface. Hence, the value of  $d_c = 4.3$  nm may reflect information on bonding dynamics as well as contact diameter. Work to understand the memory length in the context of microscopic processes is a topic of current interest [39.87].

**Test M3, Static Aging.** In this test, the block is held at  $N_b = 300$   $\mu\text{N}$  under zero spring force for a time ranging from 0.1 to 3120 s. After the hold time, the puller travels at 1  $\mu\text{m/s}$  and exerts a force  $ke$  (here  $k = 100$   $\mu\text{N}/\mu\text{m}$ ) until a slip event is observed at extension  $e_{\text{crit}}$ . The total

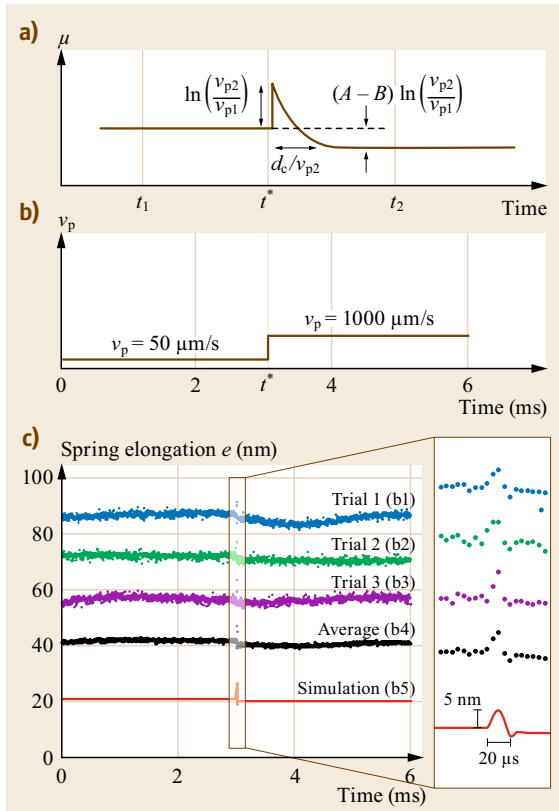


**Fig. 39.11** (a) Expected friction versus time for a velocity step. (b) Pulling velocity versus time showing a velocity step at  $t^* = 3$  ms ( $k = 100$   $\mu\text{N}/\mu\text{m}$ ,  $N_b = 15.42$   $\mu\text{N}$ ). (c) Spring elongation versus time for the pulling profile shown in (b). Multiple trials (b1)–(b3) as well as the average (b4) are shown

time is taken to be the aging time  $t_{\text{age}}$ , and the static friction coefficient  $\mu_s$  is then equal to  $ke_{\text{crit}}$ .

The resulting data is seen in Fig. 39.12, in the area annotated as *static aging trials*. Each data point is the average of about ten trials, except at the longest time of 3120 s where just three points were taken. The spread for each data point represents one standard deviation, and the dashed lines give the 95% confidence intervals for the average from a  $t$ -test. A logarithmic fit of the form  $\mu_s = \mu_0 + B \ln(t_{\text{age}}/1 \text{ s})$ , with  $B = 0.0041 \pm 0.0016$  (95% confidence) and  $R^2 = 0.80$ . Hence, at long times,  $\mu_s$  appears to be saturating. This could be indicative of the monolayer chains approaching their equilibrium configurations.

The data from Fig. 39.10 is replotted in Fig. 39.12, where time is taken to be  $d_c/v_p$ . The data from Tests M1 and M3 (dynamic and static friction measurements, respectively) extend towards each other, implying that the memory length concept applies during the sliding test. At short times,  $B = 0.024$  is a better fit to the data, supporting the idea that the aging is saturating at long times.

**Test V1, Crossing the Bifurcation Line with  $N_b$ .** In Fig. 39.8, including the effect of  $F_a$ , the bifurcation line was crossed at  $N_b \approx 2$   $\mu\text{N}$  with  $v_p = 1$   $\mu\text{m/s}$ . In Fig. 39.13, we see that at  $v_p = 50$   $\mu\text{m/s}$ , the line is crossed at  $N_b \approx 4$   $\mu\text{N}$ . This indicates a negative slope in the bifurcation line, as qualitatively indicated from Fig. 39.6b. The data now approaches the perfect stick lines, as the block has less time to creep.

**Test V2, Crossing the Bifurcation Line with  $v_p$ .** Using  $N_b = 3.45$   $\mu\text{N}$  and  $k = 10$   $\mu\text{N}/\mu\text{m}$ , we see in Fig. 39.14 that the bifurcation line is also crossed

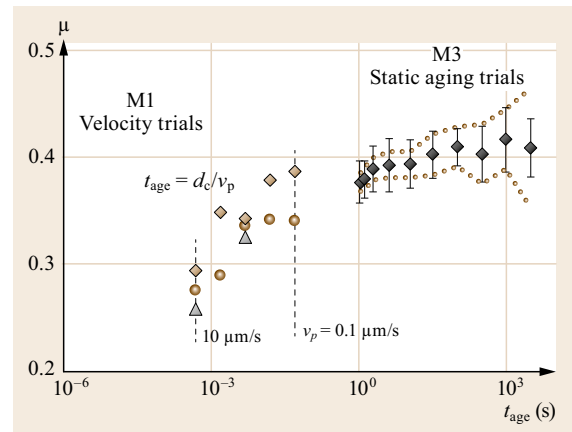


**Fig. 39.12** Results of the static aging trials, plotted alongside the results of the velocity trials shown in Fig. 39.10 with  $t_{\text{age}} = d_c/v_p$

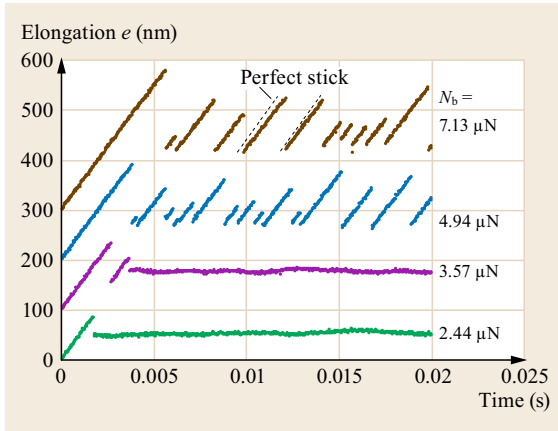


**Fig. 39.13** Elongation versus time for a fixed  $v_p = 50 \mu\text{m/s}$  and  $k = 10 \mu\text{N}/\mu\text{m}$  for increasing  $N_b$ . The camera framerate was 30 000 fps. At this  $v_p$ , a transition between stick-slip and steady sliding is seen between  $N_b = 3.57$  and  $4.94 \mu\text{N}$

between  $v_p = 30$  and  $40 \mu\text{m/s}$ . The black dashed horizontal lines indicate numerical modeling results of the maximum and minimum extensions taking the full RSF parameters and equations of motion into account. These lines indicate the average expected values. The data does show that the amplitude tends to decrease as  $v_p$  increases. The deviations from the average prediction observed in the data likely indicate that the actual topography sampled from point to point varies along the block trajectory.

**Quantitative Bifurcation Line Prediction**

The equation of motion incorporating the RSF coefficients can now be written. A perturbation on the

extension  $e$  is applied to a condition where steady sliding exists. An exponential solution is assumed for the subsequent  $e$  time dependence. Negative roots mean that there will be an oscillatory decay back to steady sliding, while positive roots indicate a divergent response and that the system will take on a stick-slip response. The bifurcation line divides these two responses. The perturbation theory result is [39.88]

$$k_{\text{crit}} = N_b \left( 1 + \frac{v_p m_b (v_p + v_c)}{N_b A d_c} \right) \times \left( \left( \frac{B}{d_c + v_p \psi_c} \right) - \left( \frac{A}{v_p + v_c} \right) \frac{v_p}{d_c} \right). \tag{39.8}$$

The values for the parameters  $A$ ,  $B$ ,  $d_c$ ,  $v_c$  and  $\psi_c$  were determined from Tests M1 and M2 as described above. For a given value of  $k$ ,  $1/N_b$  can be plotted against  $v_p$ . This has been done in Fig. 39.15 using further data from Tests V1 and V2 above. Some 20 devices, different from the ones used to determine the parameters, were used to find the bifurcation experimentally. It is seen that the experimental results agree well with the predicted curve. While this is expected from theory, experimentally this means (1) that wear is sufficiently low over the  $\approx 100$  trials needed to characterize the experimental parameters, and (2) that the parameters apply to devices other than those measured, and therefore that the kinetic phase diagram has been well quantified.

**RSF Summary**

In this section, we have seen that RSF is a useful phenomenological framework for measuring the time and velocity dependence of friction not only at the scale

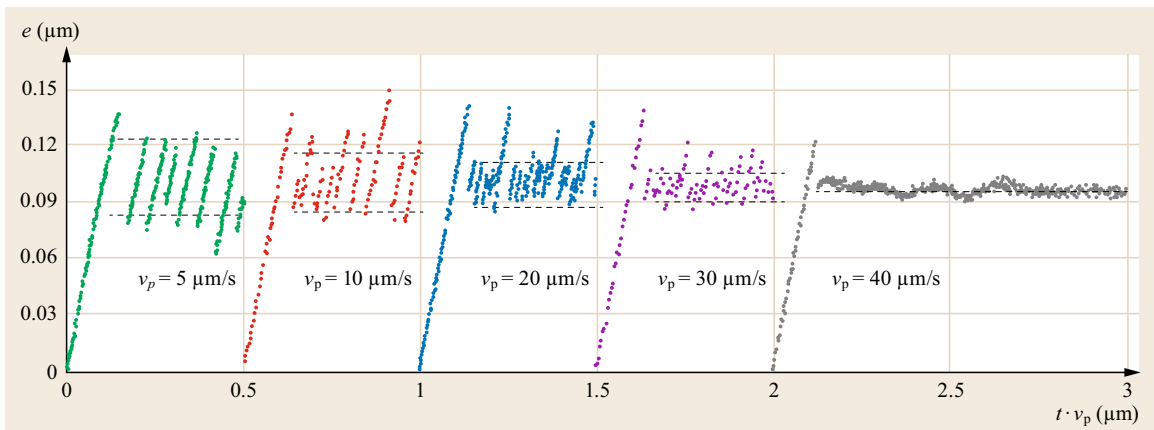


**Fig. 39.14** Spring elongation versus actuator position  $t v_p$  for a representative device at various velocities. Here  $k = 10 \mu\text{N}/\mu\text{m}$  and  $N_b = 3.45 \mu\text{N}$ . RSF simulation maximum and minimum elongations are represented by *dashed lines*

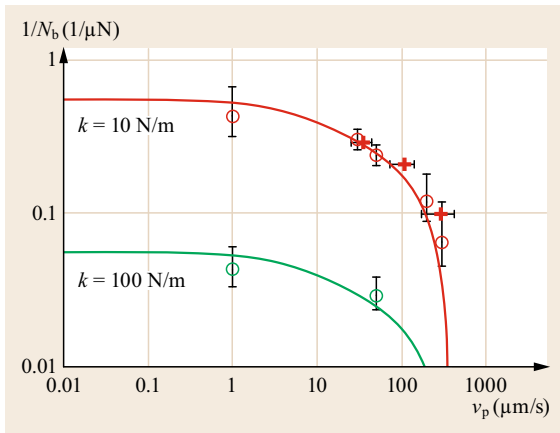


**Fig. 39.15** Predicted bifurcation lines and average experimental transition between stick-slip and steady sliding via normal load variation (circles, vertical error bars) or velocity variation (crosses, horizontal error bars). Error bars represent one standard deviation of the critical velocity or inverse normal force at which the transition occurs ◀

of earthquakes [39.89] or macroscale objects ( $\approx 1$  kg with  $\mu\text{m}$ -scale asperities) [39.66], but also at the scale of microscale objects ( $\approx 10^{-10}$  kg with nm-scale as-

perities). Although RSF predicts average friction well at the microscale, very likely only a few asperities are in contact. This gives rise to noise in the friction behavior, which requires further study. Another area of interest is the dependence of the RSF parameters on the particular monolayer chain that is applied to the surface. Although bonding across the interface may lower the free energy, the chain's entropy is also lowered. The dynamical interplay between these factors will be interesting to study. It will also be of interest to see if and how nanotribology results can be linked to RSF.

## 39.3 Putting MEMS Friction to Use: Making Motors and Friction Instruments

### 39.3.1 Microengines, Pumps and Generators

A long-held dream is to fabricate reliable gas turbine engines from MEMS technology [39.90]. Such engines would theoretically deliver a thrust to weight ratio 100 times that of their macroscale counterparts. Most of the early work in this area involved high-speed dynamics control, with engines working above 1 million rpm on a cushion of air [39.91]. These engines were fabricated from multiple layers of silicon. The design allowed no taper during very deep etches and hence the manufacturing margin was low.

More recently, Ghodssi et al. put ball bearings to use in a six-phase electric micromotor that generated  $300\ \mu\text{W}$  at 500 rpm [39.92]. One advantage of the design is that the bearings allow precise control of rotation to within a few degrees, which is important for certain sensor designs [39.93]. Another is that fabrication tolerance need not be controlled as tightly. In principle, such machines could run up to 200 000 rpm [39.93]. Microscale pumps with ball bearings have also been investigated. They could feed hydrogen or alcohol to miniaturized fuel cells for electrical generation or microturbines for torque generation. Electric generators can also be built with this technology.

In the designs, a silicon raceway surrounds stainless steel microballs of  $285\ \mu\text{m}$  diameter. Friction is characterized using a *spin-down* test [39.94]. The friction platform is schematically represented in Fig. 39.16a.

The rotor spins about the axis shown as driven by gas pressure that flow through stator vanes. The microballs enable the spinning and fill 85% of the racetrack. Normal force is provided by gas pressure through the thrust plenum flow, as shown in Fig. 39.16b. An optical probe measures radial displacement. Figure 39.16c shows spin-down data after the turbine flow is shut off. A simple friction torque model captures the data very well in this case.

Similar spin-down tests after increasing numbers of cycles (up to 200 million cycles) were used to characterize wear with raceways coated by SiC and TiN [39.95]. The SiC coating was quickly removed due to adhesive wear, and the balls adhered to the underlying silicon surface. The TiN coating wore gradually in select areas. Bare silicon raceways experienced high pressure, as evidenced by a phase change to an amorphous phase as evidenced by Raman spectroscopy. The US Army is now supporting this research. Future work will address the ball strength and study the effect of molecular monolayers.

### 39.3.2 In-situ TEM for Friction Investigations

While driven by applications such as accelerometers, gyroscopes and displays, microtechnology evolution has also been heavily leveraged to develop ever more sophisticated scientific instruments. One example is the

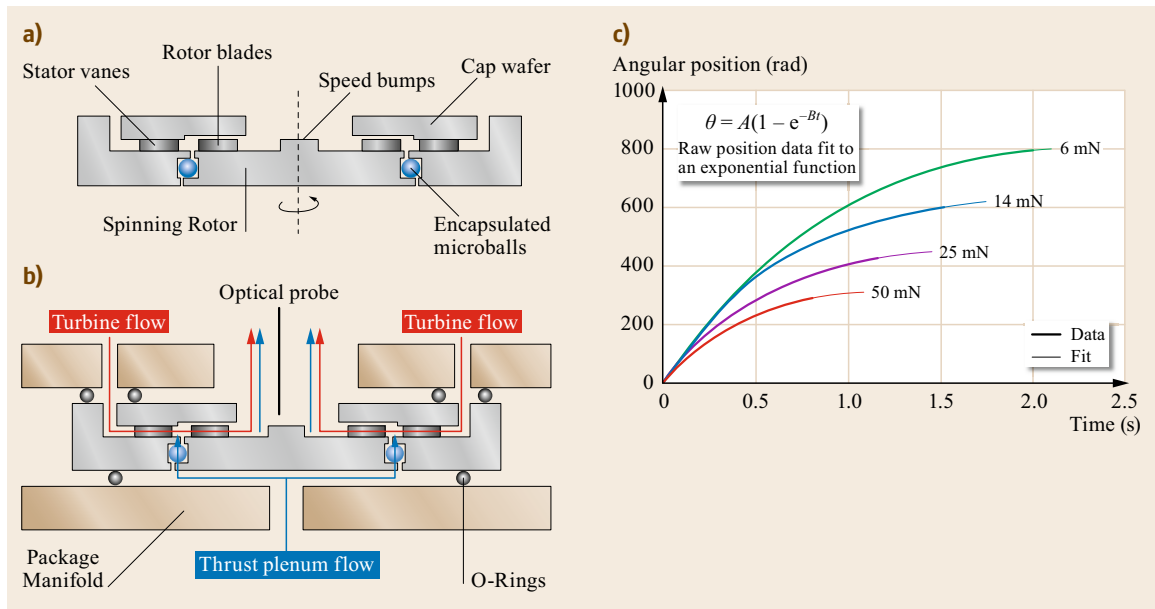


**Fig. 39.16a–c** Ball bearing friction test platform. (a) The rotor spins about the axis shown as driven by gas pressure that flow through stator vanes. The microballs enable the spinning. (b) Normal force is provided by gas pressure through the thrust plenum flow. An optical probe measures radial displacement. (c) Output data as a function of normal load from 6 to 50 mN (after [39.94])

push-to-pull indenter available from Hysitron [39.96, 97]. Transmission electron microscopy (TEM) has been applied to gain detailed images of the tips that are so widely used in FFM, both before and after use [39.98]. Wear has been analyzed by a transition state theoretical approach [39.99]. In-situ TEM friction force tools have

also been recently been constructed [39.100–102]. The MEMS in-situ TEM platform of Sato et al. [39.102] has enabled real-time TEM imaging of shearing action on a Ag-Ag nanoasperity junction. This method may allow detailed observations of shear-induced dislocation motion at the interface versus in the bulk.

## 39.4 Wear and Tribopolymer Evolution in Micro- and Nanoswitches

We now present some closing thoughts on another nanotribology issue of great current interest. Micro- and nanoswitches afford many potential advantages including high switching speeds (ns to  $\mu$ s), low power operation (aJ to nJ per cycle), and high-temperature operation. Microswitch applications envisaged include radio-frequency phased array radars [39.103] and downstream circuit breakers [39.104]. Nanoswitches are attracting attention as candidate devices to complement metal oxide semiconductor field effect transistors (MOSFETs) in digital logic [39.105, 106]. MOSFETs are limited to  $\approx 1$  V operation, and begin to leak significantly as the voltage is reduced, creating static power losses [39.107]. Some nanoswitch designs employ electrostatic actuation and can switch in 10–20 ns [39.108] at gate voltages  $< 10$  V while other designs use piezoelectric materials [39.109] and can be switched at

voltages as low as 1 mV. These devices have shown negligible off-state leakage. Significant dynamic power savings can also be realized with nanoswitches. An important challenge in commercializing *microswitches* is that the electrical contact resistance (ECR) must often remain low ( $\approx 1 \Omega$ ) and stable over  $10^8$ – $10^9$  cycles [39.103, 110]. This requirement may be relaxed for *nanoswitch* digital logic applications because even at several k $\Omega$ , mechanical delay time is large compared to electrical delay time [39.106]. However, to fulfill industry needs, they must also function reliably up to  $10^{16}$  cycles. Their low-power consumption makes them exciting candidates for sensors in the developing internet of things (IoT) devices [39.111].

Given the daunting challenge of ultrahigh cycles, fundamental insight into the underlying reliability mechanisms must be gained. One important issue is ma-

terial wear [39.113]. We close here with some thoughts on the more poorly understood issue of tribopolymer (TP) development. It is well-known from *Hernance* and *Egan* [39.114] and subsequent work [39.115] that switch resistance is sensitive to trace levels of organic vapors, which can develop into TP when subject to shear. Such vapors are typically present in the atmosphere at the parts per billion (ppb) level. Because of the nN forces and mV levels in nanoswitches, a thin adsorbed layer must be considered as a potential cause of high resistance. TPs can deposit on nearly any material from both short- and long-chain molecules [39.114].

The ambient background may play an important role in their adsorption and evolution as well. *Brand et al.* have performed tests in both  $N_2$  and  $N_2 : O_2$  ambience [39.112, 116]. Figure 39.17 shows how the ECR of vacuum-baked switches increases when cycled in 0.25% by volume benzene. For Pt-coated switches, ECR rapidly rises with cycle count in an  $N_2$  environment (Fig. 39.17a), but more slowly in  $N_2 : O_2$  (Fig. 39.17b).  $RuO_2$  is reported to be a catalytically deactivated surface [39.117] that has been used to

enhance reliability in reed relays, but in an  $N_2$  environment, ECR rises quickly (Fig. 39.17c). However, in an  $N_2 : O_2$  environment, ECR remains stable at just  $30 \Omega$  in spite of the very high benzene concentration. Much less TP was generated in the case of Fig. 39.17d compared to Fig. 39.17a–c as indicated by SEM imaging [39.112]. Bridging oxygens may act to desorb the benzene and are subsequently replenished in the  $N_2 : O_2$  atmosphere. Another important observation is that these switches were cycled under cold switching conditions, in which 5 V is applied to the contacts only after they were closed. It appears that the TP breaks down electrically and forms a graphitic layer that conducts [39.118]. In the absence of current, a thick insulating layer builds up even under repetitive normal load cycling.

Materials, environment and cycling conditions each play a significant role in micro- and nanoswitch reliability. This short overview indicates that fundamental understanding of the mechanisms leading to contact degradation may enable a tribological interface to be engineered that will meet device reliability requirements.

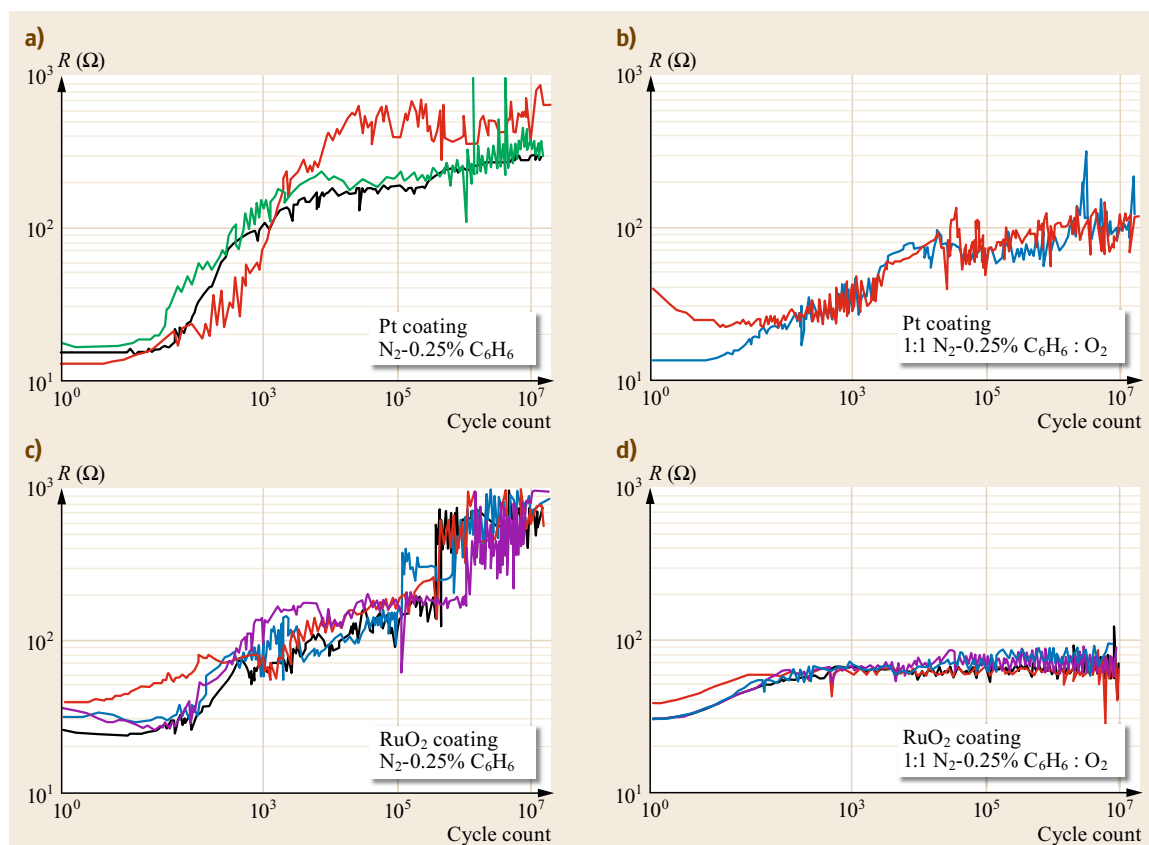


**Fig. 39.17** ECR versus cycle count for Pt and  $RuO_2$  coating in  $N_2$ -0.25%  $C_6H_6$  and 1 : 1  $N_2$ -0.25%  $C_6H_6 : O_2$  atmospheres (after [39.112])

## 39.5 Concluding Remarks

We have reviewed the background and taken a whirlwind tour of the status and recent progress in micro- and nanotribology. Understanding and solving the challenging issues in this area could enable components such as forceful linear actuators and micropowered pumps, motors and generators to come into use. Low-power switches may become integral to IoT sensors. In order to attain these goals, further progress towards a fundamental understanding of the links between interfacial shear and normal stress and the effect of intended (and unintended) lubricants is needed. Rate-state phenomenology is a promising framework for understanding friction at many length scales.

**Acknowledgments.** This work was partially supported by NSF CMMI Grants 1030322, 1030278 and 1334572. SSS was supported by the NSF Graduate Research Fellowship Program. Many of the MEMS devices discussed were fabricated by Sandia National Laboratories, Albuquerque, NM, USA. Certain commercial equipment, instruments, or materials are identified in this chapter in order to specify the experimental procedure adequately. Such identification is not intended to imply recommendation or endorsement by the National Institute of Standards and Technology, nor is it intended to imply that the materials or equipment identified are necessarily the best available for the purpose.

## References

- 39.1 M.S. Rodgers, J.J. Sniegowski: Five-level polysilicon surface micromachine technology: Application to complex mechanical systems. In: *Proc. Solid-State Sens. Actuator Workshop, Hilton Head Island* (1998) pp. 144–149
- 39.2 J.J. Sniegowski, M.P. de Boer: IC-compatible polysilicon surface micromachining, *Annu. Rev. Mater. Sci.* **30**, 299–333 (2000)
- 39.3 L. Eldada: Advances in telecom and datacom optical components, *Opt. Eng.* **40**, 1165 (2001)
- 39.4 E. Sarajlic, C. Yamahata, E. Berenschot, N. Tas, H. Fujita, G. Krijnen: High-performance shuffle motor fabricated by vertical trench isolation technology, *Micromachines* **1**, 48–67 (2010)
- 39.5 P. Vettiger, M. Despont, U. Drechsler, U. Durig, W. Haberle, M.I. Lutwyche, H.E. Rothuizen, R. Stutz, R. Widmer, G.K. Binnig: The millipede – More than one thousand tips for future AFM data storage, *IBM J. Res. Dev.* **44**, 323 (2000)
- 39.6 J.M. Zara, S.W. Smith: A micromachine high frequency ultrasound scanner using photolithographic fabrication, *IEEE Trans. Ultrason. Ferroelectr. Freq. Control* **49**, 947–958 (2002)
- 39.7 T. Akiyama, D. Collard, H. Fujita: Scratch drive actuator with mechanical links for self-assembly of three-dimensional MEMS, *J. Microelectromech. Syst.* **6**, 10 (1997)
- 39.8 E. Sarajlic: *Electrostatic Microactuators Fabricated by Vertical Trench Isolation Technology*, Ph.D. Thesis (University of Twente, Enschede 2005)
- 39.9 M. Naraghi, T. Ozkan, I. Chasiotis, S.S. Hazra, M.P. de Boer: MEMS platform for on-chip nanomechanical experiments with strong and highly ductile nanofibers, *J. Micromech. Microeng.* **20**, 125022 (2010)
- 39.10 T. Akiyama, K. Shono: Controlled stepwise motion in polysilicon microstructures, *J. Microelectromech. Syst.* **2**, 106 (1993)
- 39.11 R.J. Linderman, V.M. Bright: Nanometer precision positioning robots utilizing optimized scratch drive actuators, *Sens. Actuators A* **91**, 292 (2001)
- 39.12 N. Tas, J. Wissink, L. Sander, T. Lammerink, M. Elwenspoek: Modeling, design and testing of the electrostatic shuffle motor, *Sens. Actuators A* **70**, 171 (1998)
- 39.13 M.P. de Boer, D.L. Luck, W.R. Ashurst, A.D. Corwin, J.A. Walraven, J.M. Redmond: High-performance surface-micromachined inchworm actuator, *J. Microelectromech. Syst.* **13**, 63 (2004)
- 39.14 E. Sarajlic, E. Berenschot, H. Fujita, G. Krijnen, M. Elwenspoek: Bidirectional electrostatic linear shuffle motor with two degrees of freedom. In: *Proc. IEEE MEMS* (2005) pp. 391–394
- 39.15 G. Amontons: On the resistance originating in machines (in French), *Mém. Acad. R. A* **0**, 206–222 (1699)
- 39.16 F.P. Bowden, D. Tabor: *Friction and Lubrication of Solids: Part I* (Oxford Univ. Press, Oxford 1950)
- 39.17 H. Hertz: On the contact of elastic solids, *J. Reine Angew. Math.* **92**, 156–171 (1881)
- 39.18 K.L. Johnson, K. Kendall, A.D. Roberts: Surface energy and the contact of elastic solids, *Proc. R. Soc. A* **324**, 301 (1971)
- 39.19 B.V. Derjaguin, V.M. Muller, Y.P. Toporov: Effect of contact deformations on the adhesion of particles, *J. Colloid Interface Sci.* **53**, 314 (1975)
- 39.20 D. Tabor: Surface forces and surface interactions, *J. Colloid Interface Sci.* **58**, 2–13 (1977)
- 39.21 D. Maugis: Adhesion of spheres: The JKR–DMT transition using a Dugdale model, *J. Colloid Interface Sci.* **150**, 243–269 (1992)
- 39.22 R.W. Carpick, N. Agrait, D.F. Ogleter, M. Salmeron: Measurement of interfacial shear (friction) with an ultrahigh vacuum atomic force microscope, *J. Vac. Sci. Technol. B* **14**, 1289–1295 (1996)
- 39.23 M. Enachescu, R.J.A.V.D. Oetelaar, R.W. Carpick, D.F. Ogleter, C.F.J. Flipse, M. Salmeron: Obser-

- vation of proportionality between friction and contact area at the nanometer scale, *Tribol. Lett.* **7**, 73–78 (1999)
- 39.24 M.A. Lantz, S.J. O'Shea, M.E. Welland, K.L. Johnson: Atomic force microscope study of contact area and friction on NbSe<sub>2</sub>, *Phys. Rev. B* **55**, 10776–10785 (1997)
- 39.25 J.F. Archard: Contact and rubbing of flat surfaces, *J. Appl. Phys.* **24**, 981–988 (1953)
- 39.26 J.F. Archard: Elastic deformation and the laws of friction, *Proc. R. Soc. A* **243**, 190–205 (1957)
- 39.27 J.A. Greenwood, J.B.P. Williamson: Contact of nominally flat surfaces, *Proc. R. Soc. A* **295**, 300–319 (1966)
- 39.28 K.N.G. Fuller, D. Tabor: The effect of surface roughness on the adhesion of elastic solids, *Proc. R. Soc. A* **345**, 327 (1975)
- 39.29 D. Maugis: On the contact and adhesion of rough surfaces, *J. Adhes. Sci. Technol.* **10**, 161 (1996)
- 39.30 G. Carbone, F. Bottiglione: Asperity contact theories: Do they predict linearity between contact area and load?, *J. Mech. Phys. Solids* **56**, 2555–2572 (2008)
- 39.31 L. Pastewka, M.O. Robbins: Contact between rough surfaces and a criterion for macroscopic adhesion, *Proc. Natl. Acad. Sci. USA* **111**, 3298–3303 (2014)
- 39.32 B.N.J. Persson: On the nature of surface roughness with application to contact mechanics, sealing, rubber friction and adhesion, *J. Phys.: Condens. Matter* **17**, 1071–1142 (2005)
- 39.33 J.I. McCool: Comparison of models for the contact of rough surfaces, *Wear* **107**, 37 (1986)
- 39.34 M.G. Lim, J.C. Chang, D.P. Schultz, R.T. Howe, R.M. White: Polysilicon microstructures to characterize static friction. In: *Proc. IEEE MEMS Workshop, Napa Valley* (1990) pp. 82–88
- 39.35 W.R. Ashurst, Y.J. Jang, L. Magagnin, C. Carraro, M.M. Sung, R. Maboudian: Nanometer-thin titania films with SAM-level stiction and superior wear resistance for reliable MEMS performance. In: *Proc. 17th IEEE Int. Conf. MEMS* (2004) pp. 153–156
- 39.36 W.R. Ashurst, C. Yau, C. Carraro, C. Lee, R.T. Howe, R. Maboudian: Alkene based monolayer films as anti-stiction coatings for polysilicon MEMS, *Sens. Actuators A* **9**, 239 (2001)
- 39.37 D.C. Senft, M.T. Dugger: Friction and wear in surface-micromachined tribological test devices, *Proc. SPIE* **3224**, 31–38 (1997)
- 39.38 W.M.V. Spengen, J.W.M. Frenken: The Leiden tribometer: Real time dynamic friction loop measurements with an on-chip tribometer, *Tribol. Lett.* **28**, 149–156 (2007)
- 39.39 N.R. Tas, C. Gui, M. Elwenspoek: Static friction in elastic adhesion contacts in MEMS, *J. Adhes. Sci. Technol.* **17**, 547 (2003)
- 39.40 S.J. Timpe, K. Komvopoulos: The effect of adhesion on the static friction properties of sidewall contact interfaces of microelectromechanical devices, *J. Microelectromech. Syst.* **15**, 1612 (2006)
- 39.41 S.J. Timpe, K. Komvopoulos: Microdevice for measuring friction and adhesion properties of sidewall contact interfaces of microelectromechanical systems, *Rev. Sci. Instrum.* **78**, 065106–1–065106–9 (2007)
- 39.42 W.R. Ashurst, M.P. de Boer, C. Carraro, R. Maboudian: An investigation of sidewall adhesion in MEMS, *Appl. Surf. Sci.* **212/213**, 735–741 (2003)
- 39.43 R.W. Carpick, D.F. Ogletree, M. Salmeron: A general equation for fitting contact area and friction vs load measurements, *J. Colloid Interface Sci.* **211**, 395–400 (1997)
- 39.44 G.J. Leggett: Friction force microscopy of self-assembled monolayers: Probing molecular organisation at the nanometre scale, *Anal. Chim. Acta* **479**, 17–38 (2003)
- 39.45 Y.L. Chen, J.N. Israelachvili: Effects of ambient conditions on adsorbed surfactant and polymer monolayers, *J. Phys. Chem.* **96**, 7752 (1992)
- 39.46 J.B.D. Green, M.T. McDermott, M.D. Porter, L.M. Siperko: Nanometer-scale mapping of chemically distinct domains at well-defined organic interfaces using frictional force microscopy, *J. Phys. Chem. B* **99**, 10960–10965 (1995)
- 39.47 G.Y. Liu, P. Fenter, C.E.D. Chidsey, D.F. Ogletree, P. Eisenberger, M. Salmeron: An unexpected packing of fluorinated *n*-alkane thiols on Au(111): A combined atomic-force microscopy and x-ray diffraction study, *J. Chem. Phys.* **101**, 4301 (1994)
- 39.48 M.T. McDermott, J.B.D. Green, M.D. Porter: Scanning force microscopic exploration of the lubrication capabilities of *n*-alkanethiolate monolayers chemisorbed at gold: Structural basis of microscopic friction and wear, *Langmuir* **13**, 2504–2510 (1997)
- 39.49 E.W.V.D. Vegte, G. Hadziioannou: Scanning force microscopy with chemical specificity: An extensive study of chemically specific tip-surface interactions and the chemical imaging of surface functional groups, *Langmuir* **13**, 4357–4368 (1997)
- 39.50 Y. Liu, D.F. Evans, Q. Song, D.W. Grainger: Structure and frictional properties of self-assembled surfactant monolayers, *Langmuir* **12**, 1235–1244 (1996)
- 39.51 B.D. Beake, G.J. Leggett: Friction and adhesion of mixed self-assembled monolayers studied by chemical force microscopy, *Phys. Chem. Chem. Phys.* **1**, 3345–3350 (1999)
- 39.52 H.I. Kim, T. Koini, T.R. Koini, S.S. Perry: Systematic studies of the frictional properties of fluorinated monolayers with atomic force microscopy: Comparison of CF<sub>3</sub>- and CH<sub>3</sub>- terminated films, *Langmuir* **13**, 7192–7196 (1997)
- 39.53 E.W.V.D. Vegte, A. Subbotin, G. Hadziioannou, P.R. Ashton, J.A. Preece: Nanotribological properties of unsymmetrical *n*-dialkyl sulfide monolayers on gold: Effect of chain length on adhesion, friction, and imaging, *Langmuir* **16**, 3249–3256 (2000)
- 39.54 E.D. Reedy: Thin-coating contact mechanics with adhesion, *J. Mater. Res.* **21**, 2660–2668 (2006)

- 39.55 E.D. Reedy: Contact mechanics for coated spheres that includes the transition from weak to strong adhesion, *J. Mater. Res.* **22**, 2617–2622 (2007)
- 39.56 W.R. Ashurst, C. Yau, C. Carraro, R.M.R. Maboudian, M.T. Dugger: Dichlorodimethylsilane as an anti-stiction monolayer for MEMS: A comparison to the octadecyltrichlorosilane self-assembled monolayer, *J. Microelectromech. Syst.* **10**, 41 (2001)
- 39.57 A.D. Corwin, M.P. de Boer: Effect of adhesion on dynamic and static friction in surface micromachining, *Appl. Phys. Lett.* **84**, 2451 (2004)
- 39.58 A.D. Corwin, M.D. Street, R.W. Carpick, W.R. Ashurst, M.P. de Boer: Pre-sliding tangential deflections can govern the friction of MEMS devices. In: *Proc. ASME/STLE Jt. Int. Tribol. Conf., Long Beach* (2004)
- 39.59 E.E. Flater, A.D. Corwin, M.P. de Boer, M.J. Shaw, R.W. Carpick: In-situ wear studies of surface micromachined interfaces subject to controlled loading, *Wear* **260**, 580–593 (2006)
- 39.60 C. Carraro, O.W. Yauw, M.M. Sung, R. Maboudian: Observation of three growth mechanisms in self-assembled monolayers, *J. Phys. Chem. B* **102**, 4441 (1998)
- 39.61 E.E. Flater, W.R. Ashurst, R.W. Carpick: Nanotribology of octadecyltrichlorosilane monolayers and silicon: Self-mated versus unmated interfaces and local packing density effects, *Langmuir* **23**, 9242–9252 (2007)
- 39.62 B.G. Bush, F.W. DelRio, J. Opatkiewicz, R. Maboudian, C. Carraro: Effect of formation temperature and roughness on surface potential of octadecyltrichlorosilane self-assembled monolayer on silicon surfaces, *J. Phys. Chem. A* **111**, 12339–12343 (2007)
- 39.63 E.E. Flater, W.R. Ashurst, R.W. Carpick: Nanotribology of octadecyltrichlorosilane monolayers and silicon: Self-mated versus unmated interfaces and local packing density effects, *Langmuir* **23**, 9242–9252 (2007)
- 39.64 J.H. Dieterich: Time-dependent friction in rocks, *J. Geophys. Res.* **77**, 3690 (1972)
- 39.65 J.H. Dieterich, B. Kilgore: Implications of fault constitutive properties for earthquake prediction, *Proc. Natl. Acad. Sci. USA* **93**, 3787 (1996)
- 39.66 F. Heslot, T. Baumberger, B. Perrin, B. Caroli, C. Caroli: Creep, stick-slip and dry-friction dynamics: Experiments and a heuristic model, *Phys. Rev. E* **49**, 4973 (1994)
- 39.67 J.R. Rice, A.L. Ruina: Stability of frictional slipping, *J. Appl. Mech.* **50**, 343–349 (1983)
- 39.68 A.L. Ruina: Slip instability and state variable friction laws, *J. Geophys. Res.* **88**, 359 (1983)
- 39.69 P. Berthoud, T. Baumberger, C. G'Sell, J.-M. Hiver: Physical analysis of the state- and rate-dependent friction law: Static friction, *Phys. Rev. B* **59**, 14313 (1999)
- 39.70 T. Baumberger, C. Caroli, B. Perrin, O. Ronsin: Nonlinear analysis of the stick-slip bifurcation in the creep-controlled regime of dry friction, *Phys. Rev. E* **51**, 4005–4010 (1995)
- 39.71 Y.F. Lim, K. Chen: Dynamics of dry friction: A numerical investigation, *Phys. Rev. E* **58**, 5637–5642 (1998)
- 39.72 J.T. Desaguliers: *A Course of Experimental Philosophy*, Vol. 1 (London 1734)
- 39.73 J.H. Dieterich: Time-dependent friction and the mechanics of stick-slip, *Pure Appl. Geophys.* **116**, 790–806 (1978)
- 39.74 J. Rice, A. Ruina: Stability of steady frictional slipping, *J. Appl. Mech.* **50**, 343–349 (1983)
- 39.75 S.S. Shroff, M.P. de Boer: Constant velocity high force microactuator for stick-slip testing of micromachined interfaces, *J. Microelectromech. Syst.* **24**, 1868–1877 (2015)
- 39.76 E.T. Enikov, S.S. Kedar, K.V. Lazarov: Analytical model for analysis and design of V-shaped thermal microactuators, *J. Microelectromech. Syst.* **14**, 788–798 (2005)
- 39.77 R. Hickey, D. Sameoto, T. Hubbard, M. Kujath: Time and frequency response of two-arm micromachined thermal actuators, *J. Micromech. Microeng.* **13**, 40 (2003)
- 39.78 L. Que, J.S. Park, Y.B. Gianchandani: Bent-beam electrothermal actuators-Part I: Single beam and cascaded devices, *J. Microelectromech. Syst.* **10**, 247 (2001)
- 39.79 D.A. Bristow, M. Tharayil, A.G. Alleyne: A survey of iterative learning control, *IEEE Control Syst.* **26**, 96–114 (2006)
- 39.80 S.S. Shroff, M.P. de Boer: Full assessment of micromachine friction within the rate-state framework: Experiments, *Tribol. Lett.* (2016) doi:[10.1007/511249-016-0718-3](https://doi.org/10.1007/511249-016-0718-3)
- 39.81 M.E. Saleh, J.L. Beuth, Y.N. Picard, M.P. de Boer: In situ platform for isothermal testing of thin-film mechanical properties using thermal actuators, *J. Microelectromech. Syst.* **24**, 2008–2018 (2015)
- 39.82 M.G. Hankins, P.J. Resnick, P.J. Clews, T.M. Mayer, D.R. Wheeler, D.M. Tanner, R.A. Plass: Vapor deposition of amino-functionalized self-assembled monolayers on MEMS, *Proc. SPIE* **4980**, 238–247 (2003)
- 39.83 A.D. Corwin, M.P. de Boer: Frictional aging and sliding bifurcation in monolayer-coated micromachines, *J. Microelectromech. Syst.* **18**, 250–262 (2009)
- 39.84 J.S. Courtney-Pratt, E. Eisner: The effect of tangential force on the contact of metallic bodies, *Proc. R. Soc. A* **238**, 529 (1957)
- 39.85 F.W. DelRio, M.P. de Boer, J.A. Knapp, E.D. Reedy, P.J. Clews, M.L. Dunn: The role of van der Waals forces in adhesion of micromachined surfaces, *Nat. Mater.* **4**, 629–634 (2005)
- 39.86 S.S. Shroff, M.P. de Boer: Direct observation of the velocity contribution to friction in monolayer-coated micromachines, *Extreme Mech. Lett.* **8**, 184–190 (2016)
- 39.87 T. Hatano: Rate and state friction law as derived from atomistic processes at asperities, arXiv preprint arXiv:1512.05078 (2015)
- 39.88 S.S. Shroff, M.P. de Boer: Full assessment of micromachine friction within the rate-state frame-

- work: Theory and validation, *Tribol. Lett.* (2016) doi:10.1007/511249-016-0724-5
- 39.89 N. Lapusta, J.R. Rice: Nucleation and early seismic propagation of small and large events in a crustal earthquake model, *J. Geophys. Res.: Solid Earth* (2003) doi:10.1029/2001JB000793
- 39.90 A. Epstein, S.D. Senturia: Macro power from micro machinery, *Science* **276**, 1211 (1997)
- 39.91 L.G. Fréchet, S.A. Jacobson, K.S. Breuer, F.F. Ehrich, R. Ghodssi, R. Khanna, C.W. Wong, X. Zhang, M.A. Schmidt, A.H. Epstein: High-speed microfabricated silicon turbomachinery and fluid film bearings, *J. Microelectromech. Syst.* **14**, 141–152 (2005)
- 39.92 N. Ghalichechian, A. Modafe, M.I. Beyaz, R. Ghodssi: Design, fabrication, and characterization of a rotary micromotor supported on microball bearings, *J. Microelectromech. Syst.* **17**, 632–642 (2008)
- 39.93 J. Winters: Rolling with it: Researchers are reducing friction in MEMS devices using a very old solution in a new size, *Mech. Eng.-CIME* **131**, 22–27 (2009)
- 39.94 M. McCarthy, C.M. Waits, R. Ghodssi: Dynamic friction and wear in a planar-contact encapsulated microball bearing using an integrated microturbine, *J. Microelectromech. Syst.* **18**, 263–273 (2009)
- 39.95 B. Hanrahan, S. Misra, C.M. Waits, R. Ghodssi: Wear mechanisms in microfabricated ball bearing systems, *Wear* **326**, 1–9 (2015)
- 39.96 C. Chisholm, H. Bei, M. Lowry, J. Oh, S.S. Asif, O. Warren, Z. Shan, E.P. George, A.M. Minor: Dislocation starvation and exhaustion hardening in Mo alloy nanofibers, *Acta Mater.* **60**, 2258–2264 (2012)
- 39.97 H. Guo, K. Chen, Y. Oh, K. Wang, C. Dejoie, S.S. Asif, O. Warren, Z. Shan, J. Wu, A. Minor: Mechanics and dynamics of the strain-induced M1–M2 structural phase transition in individual VO<sub>2</sub> nanowires, *Nano Lett.* **11**, 3207–3213 (2011)
- 39.98 J. Liu, J.K. Notbohm, R.W. Carpick, K.T. Turner: Method for characterizing nanoscale wear of atomic force microscope tips, *ACS Nano* **4**, 3763–3772 (2010)
- 39.99 T.D.B. Jacobs, B. Gotsmann, M.A. Lantz, R.W. Carpick: On the application of transition state theory to atomic-scale wear, *Tribol. Lett.* **39**, 257–271 (2010)
- 39.100 A. Desai, M. Haque: A novel MEMS nano-tribometer for dynamic testing in-situ in SEM and TEM, *Tribol. Lett.* **18**, 13–19 (2005)
- 39.101 T. Ishida, Y. Nakajima, K. Kakushima, M. Mita, H. Toshiyoshi, H. Fujita: Design and fabrication of MEMS-controlled probes for studying the nano-interface under in situ TEM observation, *J. Micromech. Microeng.* **20**, 075011 (2010)
- 39.102 T. Sato, T. Ishida, L. Jalabert, H. Fujita: Development of MEMS-in-TEM setup to observe shear deformation for the study of nano-scale friction, *Tribol. Online* **6**, 226–229 (2011)
- 39.103 J.J. Yao: RF MEMS from a device perspective, *J. Micromech. Microeng.* **10**, R9 (2000)
- 39.104 C. Keimel, G. Claydon, B. Li, J.N. Park, M.E. Valdes: Microelectromechanical systems-based switches for power applications, *IEEE Trans. Ind. Appl.* **48**, 1163–1169 (2012)
- 39.105 T.-J.K. Liu, D. Markovic, V. Stojanovic, E. Alon: The relay reborn, *IEEE Spectrum* **49**(31), 39–43 (2012)
- 39.106 M. Spencer, F. Chen, C.C. Wang, R. Nathanael, H. Fariborzi, A. Gupta, H. Kam, V. Pott, J. Jeon, T.J.K. Liu, D. Markovic, E. Alon, V. Stojanovic: Demonstration of integrated micro-electro-mechanical relay circuits for VLSI applications, *IEEE J. Solid – State Circuits* **46**, 308–320 (2011)
- 39.107 S. Narendra, V. De, S. Borkar, D.A. Antoniadis, A.P. Chandraskasan: Full-chip subthreshold leakage power prediction and reduction techniques for sub-0.18 μm CMOS, *IEEE J. Solid – State Circuits* **39**, 501–510 (2004)
- 39.108 D.A. Czaplowski, G.A. Patrizi, G.M. Kraus, J.R. Wendt, C.D. Nordquist, S.L. Wolfley, M.S. Baker, M.P. de Boer: A nanomechanical switch for integration with CMOS logic, *J. Micromech. Microeng.* **19**, 085003 (2009)
- 39.109 U. Zaghoul, G. Piazza: Sub-1-volt piezoelectric nanoelectromechanical relays with millivolt switching capability, *IEEE Electron Device Lett.* **35**, 669–671 (2014)
- 39.110 G.M. Rebeiz, J.B. Muldavin: RF MEMS switches and switch circuits, *IEEE Microw. Mag.* **35**, 59–71 (2001)
- 39.111 J. Gubbi, R. Buyya, S. Marusic, M. Palaniswami: Internet of things (IoT): A vision, architectural elements, and future directions, *Future Gener. Comput. Syst.* **29**, 1645–1660 (2013)
- 39.112 V. Brand, M.S. Baker, M.P. de Boer: Impact of contact materials and operating conditions on stability of micromechanical switches, *Tribol. Lett.* **51**, 341–356 (2013)
- 39.113 R.A. Couto Jr., P.E. Kladitis, K.D. Leedy, R.L. Crane: Selecting metal alloy contact materials for MEMS switches, *J. Micromech. Microeng.* **14**, 1157–1164 (2004)
- 39.114 H.W. Hermance, T.F. Egan: Organic deposits on precious metal contacts, *Bell Syst. Tech. J.* **37**, 739–776 (1958)
- 39.115 H.P. Koidl, W.F. Rieder, Q.R. Salzmänn: Parameters influencing the contact compatibility of organic vapours in telecommunication and control switches. In: *Proc. 44th IEEE Holm Conf. Electr. Contacts* (1998) pp. 220–225
- 39.116 V. Brand, M.S. Baker, M.P. de Boer: Contamination thresholds of Pt- and RuO<sub>2</sub>-coated ohmic switches, *J. Microelectromech. Syst.* **22**, 1248–1250 (2013)
- 39.117 K. Hinohara: Reed switches. In: *Electrical Contacts: Principles and Applications*, ed. by P.G. Slade (CRC, Boca Raton 1999) pp. 535–572
- 39.118 V. Brand, M.P. de Boer: Oxygen-induced graphitization of amorphous carbon deposit on ohmic switch contacts improves their electrical conductivity and protects them from wear, *J. Micromech. Microeng.* **24**, 095029 (2014)